Mukharromah and Moon
Int J Concr Struct Mater (2024) 18:11
https://doi.org/10.1186/s40069-023-00641-0

International Journal of Concrete Structures and Materials

RESEARCH

Open Access

Steel Fiber Orientation Efficiency Factor Model for a Magnetically Treated Cement-Based Composite

Nur Indah Mukharromah[1] and Do Young Moon[1*]

Abstract

In typical steel fiber-reinforced concrete, the fibers are randomly distributed and oriented throughout the matrix, and a magnetic field can effectively align these randomly oriented fibers. To predict the extent to which the steel fibers contained in mortar can be aligned by a magnetic field, an analytical steel fiber orientation efficiency factor model was proposed as a function of the magnetic induction intensity and exposure time. To verify the applicability of the proposed model, experiments were conducted for various magnetic induction intensities and exposure times with normal mortars and mortars in which some or all the sand was replaced with steel slag. The experimental results demonstrate that the proposed model allows predicting the degree of alignment of steel fibers under magnetic fields. However, this model can only be applied to a normal mortar. In the case of mortar containing steel slag, it is confirmed that the steel slag, which is a ferrous material, reduces the magnetic induction intensity, reducing the degree of alignment of steel fibers in the mortar.

Keywords Magnetic field, Steel fiber, Mortar, Orientation efficiency factor, Steel slag

1 Introduction

Steel fiber-reinforced concrete (SFRC) has been employed in a wide range of applications, including tunnel linings, slabs, pavements, and bridge deck overlays (Alavizadeh-Farhang & Silfwerbrand, 2000; Baun, 1993; Hrynyk & Vecchio, 2014; Namli, 2021). Over the last few decades, numerous researchers have thoroughly investigated the mechanical properties of SFRC (Kazemi et al., 2007; Kim et al., 2015; Madandoust et al., 2019; Valdez Aguilar et al., 2021). Steel fibers in a concrete matrix primarily change the material characteristics from quasi-brittle to pseudo-ductile, resulting in fewer catastrophic failures by bridging micro- and macro-cracks (Khan et al., 2022). In typical SFRC, steel fibers are randomly distributed and oriented throughout the matrix, uniformly dispersing their reinforcement efficiency in all directions. Despite the reinforcement, the random distribution of discrete steel fibers within concrete members decreases the efficiency of the steel fiber orientation on the member tension behavior. The orientation efficiency is significantly increased by using continuous steel fibers aligned parallel to the member tension stress direction. Therefore, a method for aligning the fibers with the major tensile-stress direction in concrete must be developed (Mu et al., 2018).

Currently, two basic methods are used to align steel fibers in SFRC: the magnetic field and flow induction methods. Miller and Bjorklund (1977) were granted a patent for using a magnetic field to align ferromagnetic fibers in freshly poured concrete slabs by passing the fibers through a rectangular coil. This method was first developed and patented by Svedberg (2004) for the alignment of fibers in a wider range of applications, such as

Journal information: ISSN 1976-0485 / eISSN 2234-1315.

*Correspondence:
Do Young Moon
dymoon@ks.ac.kr
[1] Department of Civil Engineering, Kyungsung University, 309 Suyeong-Ro, Nam-Gu, Busan 608-736, Republic of Korea

large slabs and pavements cast in situ, after successful testing on relatively small samples. Michels and Gams (2016) performed bending tests and found that samples with fibers well aligned using a magnetic field showed a better energy absorption capacity than samples with randomly oriented fibers. In contrast, using the flow induction method, Moon and Kang (2018) found that fiber orientation and distribution primarily occurred within a short flow distance, whereas Song et al. (2018) discovered that the influence of casting height on fiber distribution was more significant than the effects of flow distance and matrix rheology. Moreover, Huang et al. (2021) developed an L-shaped device to manufacture ultra-high-performance concrete with a desirable fiber orientation. The results showed that compared to the standard casting method, the flow induction method produced 35% greater fiber orientation and 30–60% higher flexural strength.

Currently, the magnetic-field method is the most extensively used method for preparing aligned SFRC. Mu et al. (2015) used an external uniform electromagnetic field to align steel fibers in cement-based composites. The results showed that the steel fiber orientation efficiency (SFOE) factor in aligned SFR cement-based composites was approximately 0.9, compared with the SFOE factor for a random distribution of steel fibers, which was approximately 0.5. Ghailan and Al-Ghalib (1971) used an electromagnetic field supplemented by vibrations to align steel fibers in self-compacting concrete. According to the findings, aligned fibers exhibited a fiber orientation factor between 0.8 and 0.95, in contrast to 0.3 and 0.5 for randomly spread fibers. Mu et al. (2015) and Ghailan and Al-Ghalib (1971) performed force analyses of a single steel fiber in a cement-based matrix to prepare aligned steel-fiber cement-based composites. Mu et al. (2015) developed an equation that can only be used to determine the magnetic induction intensity required to align steel fibers in the desired direction. More recently, Ghailan and Al-Ghalib (1971) presented a force analysis to determine whether the steel fiber aligns under magnetic field exposure.

The aforementioned studies demonstrated that a magnetic field can effectively align randomly oriented fibers in cement-based composites. The SFOE factor, η, which is the ratio of the projected length along the desired orientation to the actual length of the steel fibers, is commonly used to assess the efficiency of steel fiber reinforcement. According to this definition, steel fibers parallel to the desired orientation exhibit an SFOE factor of 1, whereas steel fibers perpendicular to the desired orientation exhibit an SFOE factor of 0. For inclined steel fibers, the SFOE factor is in the range 0–1. Several researchers have proposed theoretical models for predicting the SFOE factor in cement-based composites (Dupont & Vandewalle, 2005; Laws, 1971; Lee et al., 2014; Soroushian & Lee, 1990). However, these models were primarily designed for SFR cement-based composites. The development of a prediction model for an aligned SFR cement-based composite that considers the magnetic induction intensity and plastic viscosity parameters is insufficient. It is necessary to conduct further research on the magnetic induction intensity and plastic viscosity parameters that determine the SFOE factor. In fact, the SFOE factor for a specimen exposed to a magnetic field cannot be calculated using the typical SFOE factor models. To overcome these drawbacks, a method for predicting a SFOE factor was developed. This study was developed to address this gap by proposing a SFOE factor prediction model for magnetically treated cement-based composites. An experimental investigation was conducted to examine the SFOE factor on different types of mortar specimens exposed to an electromagnetic field and to validate the proposed model by comparing it to the experimental values.

2 Method to Obtain the Orientation Efficiency Factor

The orientation of the steel fibers in a fresh cement-based matrix can be modified and controlled by applying an external magnetic field. Owing to the driving force of the magnetic field, the steel fiber always tends to rotate in the same direction as the magnetic field. Consequently, the steel fibers in the cement-based composite can be aligned in the desired direction if the magnetic field is oriented in the same direction. The distributed magnetic field strength (f_m), gravity force (F_g), buoyancy force (F_b), and distributed viscous resistance strength (f_r) act on the steel fiber in the cement-based matrix as it rotates in a magnetic field, as illustrated in Fig. 1. To achieve directional rotation of steel fibers, the magnetic field must overcome the effects of gravity, buoyancy, and viscous resistance. To simplify the analysis, the steel fibers are assumed to be slender and uniformly cylindrical.

The distributed magnetic field strength acting on a steel fiber can be determined using Eq. (1) (Mu et al., 2017), in accordance with electromagnetism. The distributed viscous resistance strength experienced by a steel fiber in the cement-based matrix can be calculated using Eq. (2), based on the falling-cylinder viscometer concept developed by Lohrenz et al. (1960), Ashare and Lescarboura (1965), Eichstadt and Swift (1966), and Chen et al. (1968).

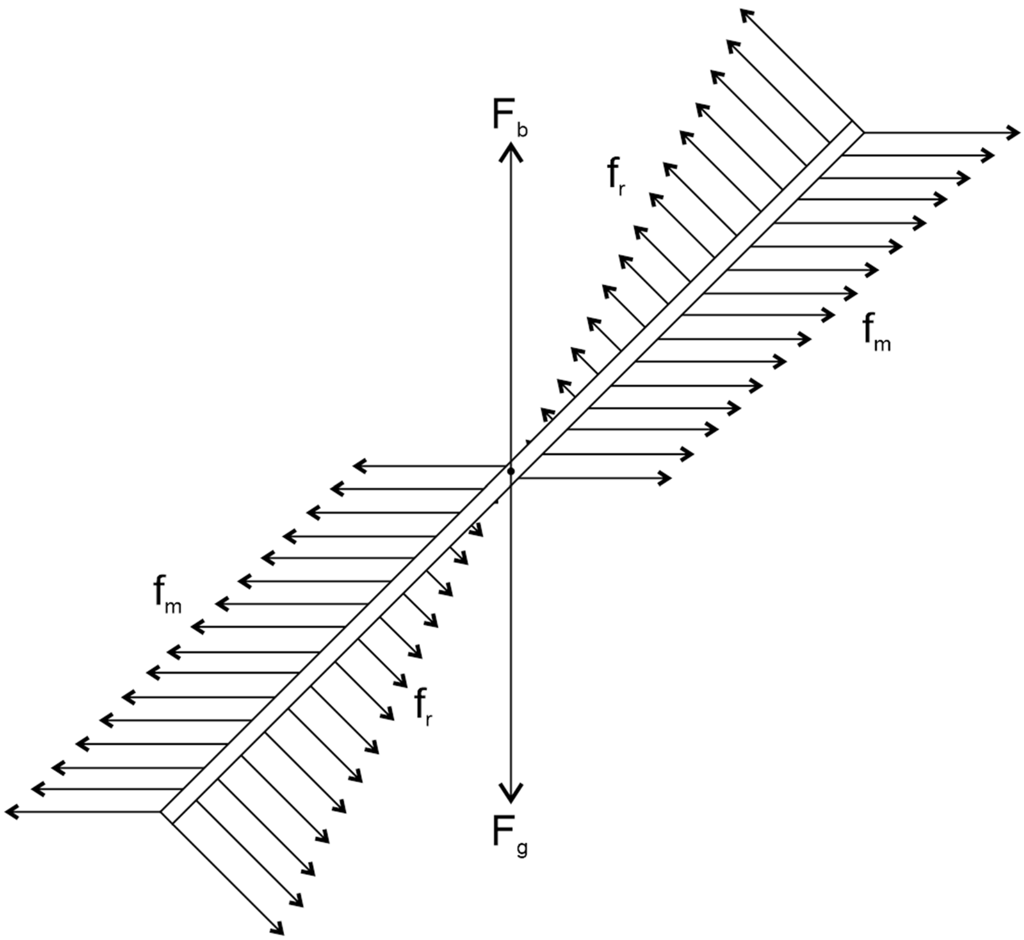

Fig. 1 Forces acting on a steel fiber under a magnetic field

$$f_m = \frac{(\mu_r - 1)B^2 A}{2\mu_0 \mu_r l} \tag{1}$$

$$f_r = k\pi\delta\alpha t l \tag{2}$$

where A is the steel fiber cross-section area (m^2), B is the magnetic induction intensity (N/(A m)), l is the steel fiber length (m), μ_0 is the vacuum permeability (N/A^2) which is typically $4\pi \times 10^{-7}$ N/A^2, $\mu_r = \mu_f/\mu_0$ is the relative permeability, μ_f is the steel fiber permeability (N/A^2) which equals $10^4\mu_0$, as reported by Ghailan and Al-Ghalib (1971), δ is the matrix plastic viscosity (Pa s), α is the angular acceleration (rad/s^2), t is the magnetic field exposure time (s), and k is the size coefficient, presented in Eq. (3).

$$k = -\frac{1 - \frac{d_f}{d_s}^2}{1 - \frac{d_f}{d_s}^2 - \left(1 + \frac{d_f}{d_s}^2\right) ln\left(\frac{d_s}{d_f}\right)} \tag{3}$$

where d_f is the steel fiber diameter (mm), and d_s is the specimen diameter (mm).

This study assumes a uniform mass distribution of the steel fibers. Therefore, the moment resulting from the gravity and buoyancy forces acting on the middle length of the steel fiber can be considered as 0, according to the moment of momentum theorem. Therefore, gravity and buoyancy forces do not affect the direction of the steel fiber rotation. Based on the momentum theorem expressed in Eq. (4), the angular acceleration (α) acting on a steel fiber in a cement-based matrix is expressed in Eq. (5).

$$J\alpha = \sum M_O = \int_0^{\frac{l}{2}} \left(f_m \cos\theta_i - f_r\right) x dx \tag{4}$$

$$\alpha = \frac{1.5(\mu_r - 1)B^2 A \cos\theta_i}{\mu_r \mu_0 l(m + 3k\pi\delta t l)} \tag{5}$$

Table 1 Experimental program variables

Mortar type	Compaction process	Magnetic induction intensity (G)	Magnetic field exposure time (s)	Test specimen label
NM	No	–	–	NM_X
	Yes	–	–	NM_O
	Yes	62.66	300	NM_O_0.25MF_1ET
	Yes	125.31	300	NM_O_0.5MF_1ET
	Yes	250.62	75	NM_O_1MF_0.25ET
	Yes	250.62	150	NM_O_1MF_0.5ET
	Yes	250.62	300	NM_O_1MF_1ET
NSSM	No	–	–	NSSM_X
	Yes	–	–	NSSM_O
	Yes	62.66	300	NSSM_O_0.25MF_1ET
	Yes	125.31	300	NSSM_O_0.5MF_1ET
	Yes	250.62	75	NSSM_O_1MF_0.25ET
	Yes	250.62	150	NSSM_O_1MF_0.5ET
	Yes	250.62	300	NSSM_O_1MF_1ET
SSM	No	–	–	SSM_X
	Yes	–	–	SSM_O
	Yes	62.66	300	SSM_O_0.25MF_1ET
	Yes	125.31	300	SSM_O_0.5MF_1ET
	Yes	250.62	75	SSM_O_1MF_0.25ET
	Yes	250.62	150	SSM_O_1MF_0.5ET
	Yes	250.62	300	SSM_O_1MF_1ET

Table 2 Material properties of fine aggregate

Material type	Absolute dry density (g/cm^3)	Surface dry density (g/cm^3)	Moisture absorption (%)	Fineness modulus	Mass density (kg/m^3)
Steel slag	3.56	3.57	0.42	3.16	2.263
Sand	2.57	2.58	0.60	3.98	1.575

where $J = \frac{1}{12}ml^2$ is the moment of inertia for a long cylinder rotating in the middle length (kg m^2), M_O is the moment resultant at the steel fiber middle length, x is the distance from the centroid of the steel fiber length, m is the mass of steel fiber (kg), θ_i is the initial angular position, or the angle between the steel fiber initial position and the plane that is perpendicular to the magnetic field direction.

As reported by Dupont and Vandewalle (2005), normal SFRC has an SFOE factor of 0.5, or an initial angular position of approximately 30°. Therefore, in this study, for the SFOE factor model, it is assumed that the steel fiber has already rotated 30° from the plane perpendicular to the direction of the magnetic field. Using constant acceleration, as shown in Eq. (6), the final angular position, or the angle between the steel fiber final position and the plane perpendicular to the magnetic field direction (θ_f) is expressed in Eq. (7). Then, according to Eq. (8) from Dupont and Vandewalle (2005) and the assumption that all the steel fibers have the same final position, the SFOE factor (η_p) can be determined as expressed in Eq. (9).

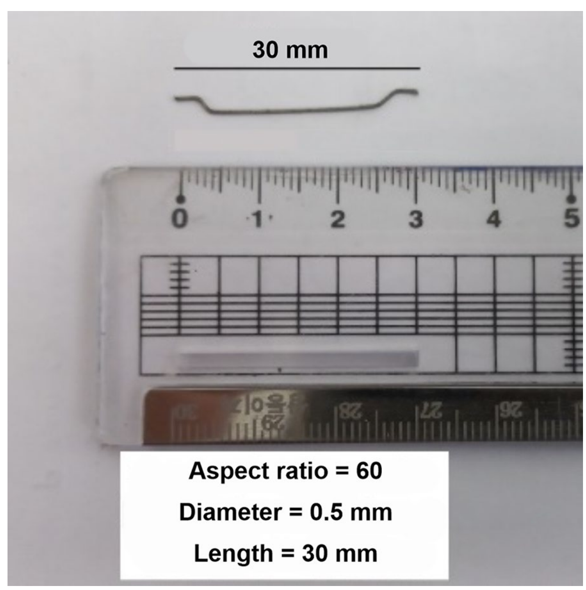

Fig. 2 Hooked-end steel fiber

Table 3 Mix proportions of the mortars

Mix type	Cement (kg/m^3)	Water (kg/m^3)	Sand (kg/m^3)	Steel slag (kg/m^3)
NM	865	364	939	–
NSSM	865	364	469	469
SSM	865	364	–	939

Table 4 Measurement of rheological properties

Mix type	Plastic viscosity (Pa s)	Yield stress (Pa)	Confidence fit (%)
NM	6.41 (±0.36)	124.77 (±4.11)	99.24 (±0.58)
NSSM	5.43 (±0.35)	77.86 (±1.58)	98.81 (±0.87)
SSM	4.10 (±0.41)	55.42 (±5.27)	97.22 (±1.84)

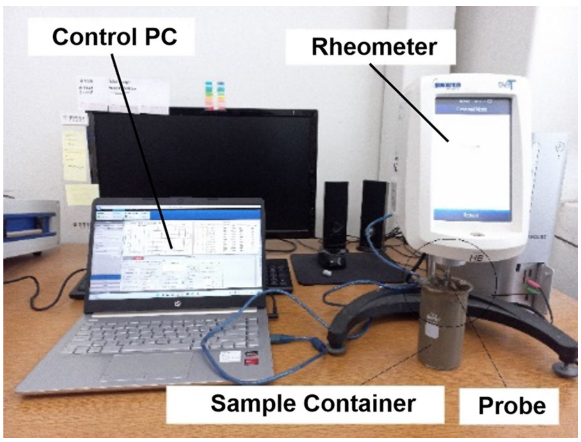

Fig. 3 Setup for rheological measurements

Fig. 5 Steel fiber placement

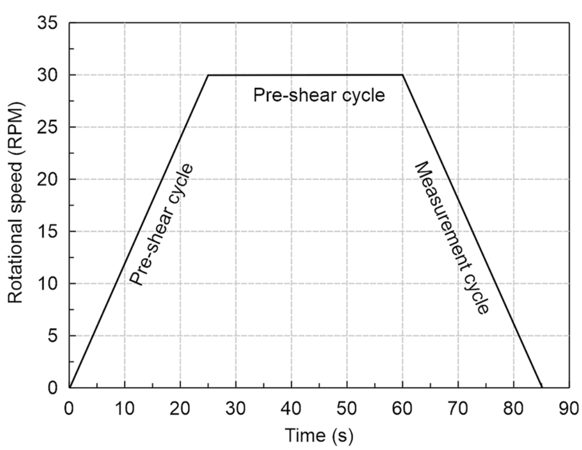

Fig. 4 Probe rotational speed control

$$\theta_f = \theta_i + \omega_i t + \frac{1}{2}\alpha t^2 \tag{6}$$

$$\theta_f = 30^\circ + \frac{1}{2}\frac{3(\mu_r - 1)B^2 A cos30^\circ t^2}{2\mu_r\mu_0 l(m + 3k\pi\delta tl)} \tag{7}$$

$$\eta_m = \frac{1}{N}\sum_i^N \cos\theta \tag{8}$$

$$\eta_p = \begin{cases} cos\left(90^\circ - \theta_f\right) & if\ \theta_f < 90^\circ \\ 1 & if\ \theta_f \geq 90^\circ \end{cases} \tag{9}$$

where ω_i is the initial angular velocity (0 rad/s), N is the number of steel fibers, and θ is the angle between the magnetic field direction and final position of the steel fiber (90°—θ_f).

If the steel fibers are already aligned in the direction of the magnetic field, they will not move under the influence of the magnetic field. Therefore, if the final angular position is greater than 90°, the SFOE factor is 1.

Using Eqs. (5) and (6), the required magnetic induction intensity (B_{req}) can be obtained as expressed in Eq. (10). This equation can be used to calculate the magnetic induction intensity required to align the steel fibers in the desired direction from their initial positions during the selected magnetic field exposure time.

$$B_{req} = \sqrt{\frac{4\mu_r\mu_0 l\left(\theta_f - \theta_i\right)(m + 3k\pi\delta tl)}{3(\mu_r - 1)A\ cos\theta_i t^2}} \tag{10}$$

3 Experimental Program for Verification

3.1 Overview

The purpose of the experimental program was to verify the proposed SFOE factor model. The experimental program variables, listed in Table 1, were selected to

Fig. 6 Exposure to the electromagnetic field

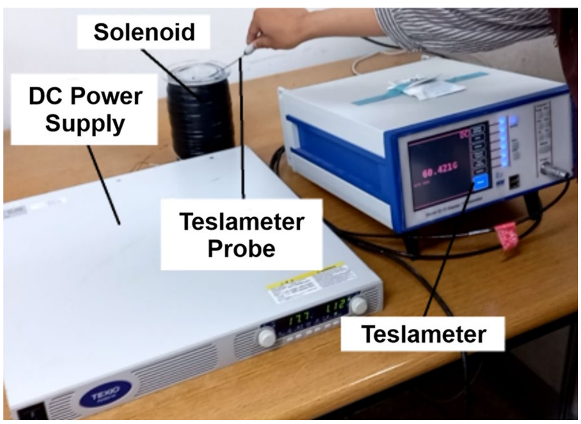

Fig. 7 Magnetic induction intensity measurements

investigate the effects of the mortar mix type, magnetic field exposure time, and magnetic induction intensity when exposed to a magnetic field. Three specimens were prepared for each variable, and a total of 63 specimens were fabricated and tested. For the mortar mix type, three reference mortar mixes were prepared: no sand composition substitution (NM), 50% sand composition substitution with steel slag (NSSM), and 100% sand composition substitution with steel slag (SSM). As steel slag is ferrous, the mobility of NSSM and SSM, which contain steel slag, is expected to increase under an applied magnetic field, which can be beneficial to creating space for steel fiber alignment. This is the reason for choosing NSSM and SSM as experimental variables. Two non-magnetically treated specimens and five magnetically treated specimens were prepared for each reference mortar mix to examine the effects of vibration compaction and magnetic field exposure. A detailed description of the vibration compaction and exposure to electromagnetic fields is presented in Sect. 3.2.3. The labels of the test specimens were arranged in the following order: mortar type, vibration compaction, magnetic-field intensity, and magnetic-field exposure time. The magnetic induction intensity and exposure time required to align the steel fibers in the direction of the magnetic field were calculated using Eq. (10) as 250.62 G and 300 s, respectively. In particular, the SFOE factor becomes 1 under these magnetic field exposure conditions. In the labels in Table 1, the intensity and exposure time are presented as ratios for these conditions (250.62 G and 300 s, respectively).

3.2 Materials and Methods

3.2.1 Materials and Mix Proportions

Type I ordinary Portland cement (KS L 5201) was used in this study, with a density of 3.15 g/cm^3. Siliceous sand and steel slag with a maximum particle size of 2 mm were employed as fine aggregate without a particular particle size distribution design. Table 2 lists the material properties of the fine aggregate. According to the manufacturer, steel slag contains approximately 40% calcium oxide, 35% silica, 13% alumina, and 8% magnesia. Fig. 2 shows the hooked-end steel fibers used in this study, with diameter (d_f), length (l), and aspect ratio (l/d_f) of 0.5 mm, 30 mm, and 60, respectively. The reported tensile strength and elastic modulus of the fibers were 1250 MPa and 200 GPa, respectively. Fifteen hooked-end steel fibers were added to each specimen and arranged horizontally at the mid-height surface of the specimen. The reference mortar mix proportions are listed in Table 3 with a water-to-cement ratio of 0.42.

3.2.2 Fresh Mortar Rheology

The drag force depends on the mortar viscosity. Consequently, the SFOE factor of the steel fibers in the

Table 5 Magnetic induction intensity measurements

Electric current (ampere)	Magnetic induction intensity (Gauss)			Average (Gauss)	Applied current for label
	Upper side	Middle height	Lower side		
1.12	51.650	62.998	51.650	55.433	0.25MF
2.23	103.006	125.637	103.006	110.550	0.5MF
4.45	205.872	251.104	205.872	220.949	1MF

Fig. 8 Specimen cutting line

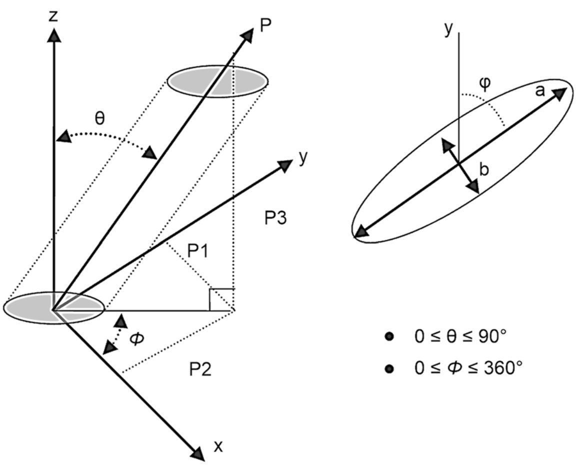

Fig. 9 Steel fiber orientation analysis

mortar is also influenced by the viscosity of the mortar. The viscosities of the NM, NSSM, and SSM mortars were measured using a Brookfield DV3T vane-rotation-type rheometer. The test setup used to determine the viscosity of the mortar mix is shown in Fig. 3.

The mortar mixes were quickly transferred to sample containers after mixing. As illustrated in Fig. 4, the rotational speed of the probe was regulated over time by adjusting the height of the probe submergence in the sample. The pre-shear cycle process ensured that each evaluated mortar sample had the same shear history. One data point was recorded every 5 s during the data recording cycle. The shear stress (τ) and shear rate (γ) data of the down curves were fitted using the Bingham model as presented in Eq. (11).

$$\tau = \tau_0 + \delta\gamma \tag{11}$$

where τ_0 is the yield stress (Pa) and δ is the plastic viscosity (Pa s).

Table 4 lists the plastic viscosity, yield stress, and confidence fit for each mortar. As presented in the table, NSSM and SSM have lower plastic viscosity compared to NM mortar. This could be the result of the high density of the steel slag, which resulted in the high amount of water in the mix for NSSM and SSM.

3.2.3 Specimen Casting and Magnetic Field Exposure

Specimens were fabricated using a casting process that included vibration compaction, magnetic field exposure, and curing. To cast a cylindrical specimen of approximately 66 mm in diameter and 140 mm in length, an acrylic mold was prepared. After filling half of the mold with mortar and compacting it on a shaking table for 60 s for vibration, as shown in Fig. 5, 15 steel fibers were placed horizontally on the mortar surface. Fifteen steel fibers are the maximum that can be placed by hand in a cross section of 66 mm diameter without overlapping steel fiber. The remaining half of the mold was then poured. The mold was then placed on the shaking table again for 60 s for vibration compaction.

For the purpose of magnetic field exposure, a hollow cylindrical plastic bobbin was fabricated, with a height of 150 mm, and inner and outer diameters of 75 and 80 mm, respectively. A solenoid chamber was fabricated by winding 1500 times a coil with a diameter of 0.8 mm around the plastic bobbin and covering it with black tape for protection. To generate a magnetic field inside the solenoid chamber, both ends of the coil were connected to a DC power supply and a current was applied to complete the magnetic field exposure process, as shown in Fig. 6.

The current applied to the solenoid chamber was determined using the previously performed measurement to obtain the required intensity of the magnetic field, as specified in Table 1. As shown in Fig. 7, the intensity of the magnetic field induced around the solenoid chamber was measured based on the applied current. While gradually increasing the current of the DC power supply, the intensity of the electromagnetic field induced at the top, middle, and bottom of the solenoid chamber was measured using a Tesla meter. Table 5 presents the current values corresponding to magnetic induction intensities close to those listed in Table 1.

After magnetic field exposure, the mold was carefully removed from the solenoid chamber and left indoors for 24 h. The specimens were then demolded and cured in water for 7 days.

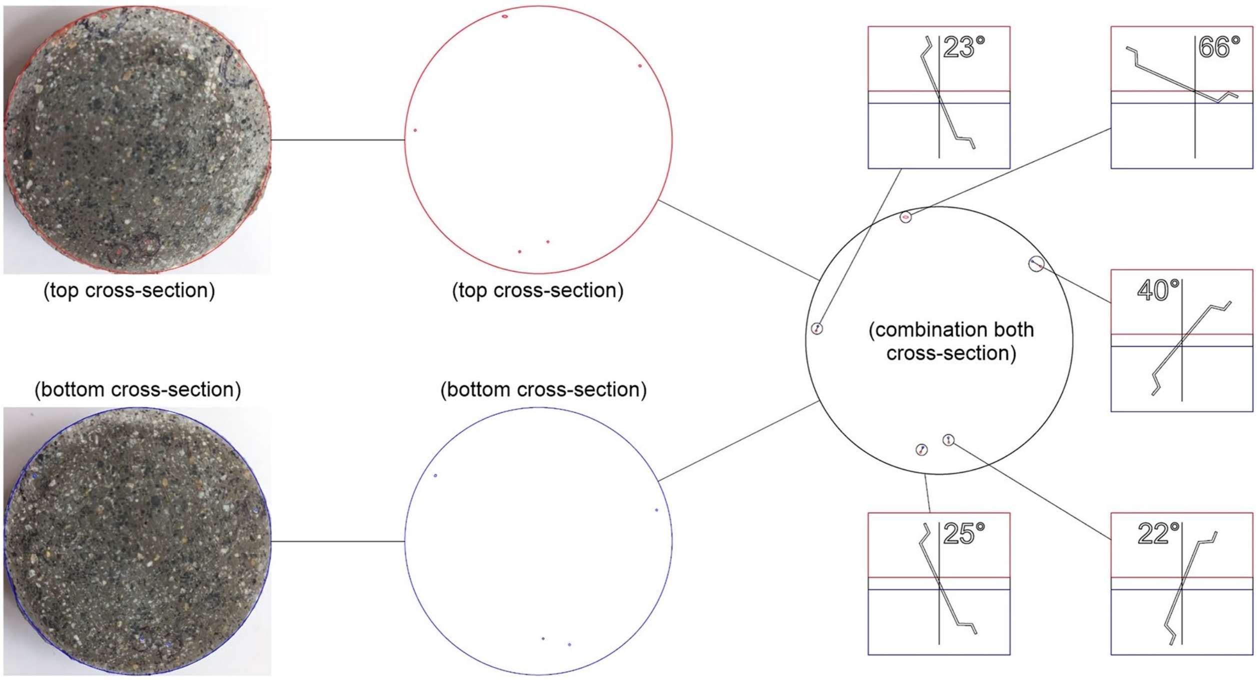

Fig. 10 Analysis of the two closest cross sections due to cut process

Table 6 SFOE factor η_m obtained from the experimental program

Mortar type	NM_			NSSM_			SSM_		
	η_m	Avg	SD	η_m	Avg	SD	η_m	Avg	SD
_X	0.28	0.27	0.05	0.28	0.30	0.05	0.33	0.35	0.02
	0.22			0.35			0.36		
	0.32			0.25			0.36		
_O	0.51	0.54	0.03	0.54	0.56	0.03	0.58	0.56	0.02
	0.57			0.54			0.54		
	0.54			0.59			0.57		
_O_0.25MF_1ET	0.56	0.58	0.04	0.65	0.60	0.04	0.54	0.49	0.06
	0.55			0.57			0.49		
	0.63			0.58			0.43		
_O_0.5MF_1ET	0.75	0.59	0.16	0.45	0.61	0.18	0.55	0.51	0.05
	0.44			0.58			0.46		
	0.57			0.81			0.53		
_O_1MF_0.25ET	0.65	0.67	0.07	0.55	0.63	0.08	0.55	0.53	0.02
	0.62			0.71			0.51		
	0.75			0.63			0.52		
_O_1MF_0.5ET	0.66	0.75	0.11	0.53	0.64	0.12	0.58	0.57	0.04
	0.87			0.76			0.52		
	0.73			0.62			0.60		
_O_1MF_1ET	0.90	0.84	0.06	0.69	0.65	0.11	0.58	0.63	0.05
	0.84			0.53			0.66		
	0.79			0.74			0.66		

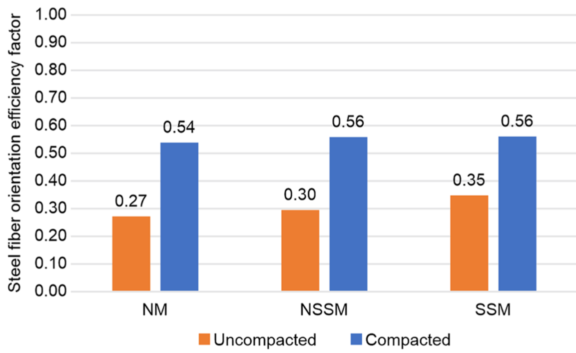

Fig. 11 Effect of compaction process on SFOE factor

Table 7 Comparison of the orientation efficiency factors for the control specimen

Present study	Soroushian and Lee (1990)	Dupont and Vandewalle (2005)	Lee et al. (2014)
0.54(NM) 0.56(NSSM) 0.56(SSM)	0.54	0.51	0.63

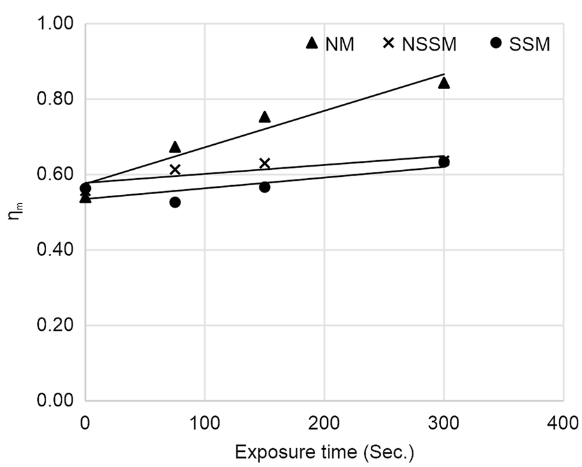

Fig. 12 Effect of magnetic field exposure time on the SFOE factor

A test specimen corresponding to "No" in the "Compaction Process" column of Table 1 is a test specimen that was neither compacted nor exposed to a magnetic field. Therefore, it can be seen that compaction and exposure to magnetic fields did not affect the results of the SFOE factor obtained from this "No" test specimen.

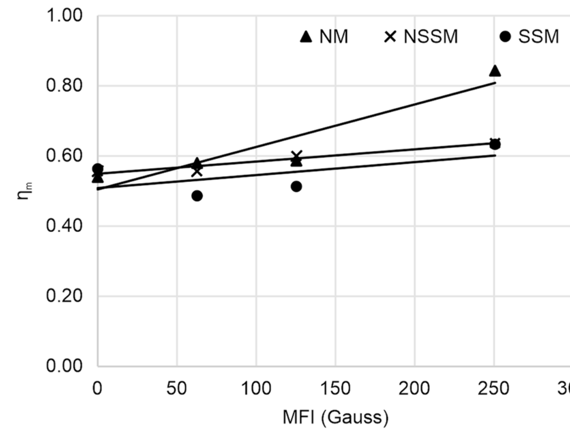

Fig. 13 Effect of the magnetic induction intensity on the SFOE factor

3.2.4 Visual Inspection Process for the SFOE Factor

At the age of 7 days, using a concrete cutter with a thickness of 3 mm, the specimens were cut into six parts (ten investigated cross sections) along the specimen height in the transverse direction, as illustrated in Fig. 8. Following Sebaibi et al. (2014), the angle between the steel fiber and the specimen cross-section axis (θ) was measured using a manual visual inspection method to examine the SFOE, as presented in Fig. 9.

Ideally, the steel fiber should be seen as a full circle when it is perpendicular to the cross-section, or else as an ellipse. The major axis length (a) and minor axis length (b) of the steel fiber in the cross-section can be used to calculate the out-of-plane angle (θ), as expressed in Eq. (12). Subsequently, in accordance with Dupont and Vandewalle (2005), Eq. (8) can be used to calculate the SFOE factor (η) of the specimen. Two adjacent cross sections must be matched with each other for the possibility of steel fiber bridging both cross sections, as shown in Fig. 10. The out-of-plane angle of the nonvisible steel fiber was considered to be 69°–70° based on the actual length of the analyzed specimen. The SFOE factors obtained from the experimental program are listed in Table 6 for all series.

$$\theta = arc \cdot \cos\left(\frac{b}{a}\right) \tag{12}$$

Table 8 Comparison of predicted and experimental factors

Mortar type	Specimen series	Parameter					η		$\frac{\eta_m}{\eta_p}$
		B_{req}	I	B_m	t	δ	η_m	η_p	
NM	NM_O	–	–	–	–	6.41	0.54	0.50	0.93
	NM_O_0.25MF_1ET	62.66	1.12	55.433	300	6.41	0.58	0.56	0.97
	NM_O_0.5MF_1ET	125.31	2.23	110.550	300	6.41	0.59	0.71	1.20
	NM_O_1MF_0.25ET	250.62	4.45	220.949	75	6.41	0.67	0.71	1.06
	NM_O_1MF_0.5ET	250.62	4.45	220.949	150	6.41	0.75	0.87	1.16
	NM_O_1MF_1ET	250.62	4.45	220.949	300	6.41	0.84	0.94	1.12
	Total average								1.07
	Standard deviation								0.10
NSSM	NSSM_O	–	–	–	–	5.43	0.56	0.50	0.89
	NSSM_O_0.25MF_1ET	62.66	1.12	55.433	300	5.43	0.60	0.57	0.95
	NSSM_O_0.5MF_1ET	125.31	2.23	110.550	300	5.43	0.61	0.74	1.21
	NSSM_O_1MF_0.25ET	250.62	4.45	220.949	75	5.43	0.63	0.74	1.17
	NSSM_O_1MF_0.5ET	250.62	4.45	220.949	150	5.43	0.64	0.91	1.42
	NSSM_O_1MF_1ET	250.62	4.45	220.949	300	5.43	0.65	1	1.54
	Total average								1.20
	Standard deviation								0.23
SSM	NM_O	–	–	–	–	4.10	0.56	0.50	0.89
	SSM_O_0.25MF_1ET	62.66	1.12	55.433	300	4.10	0.49	0.59	1.20
	SSM_O_0.5MF_1ET	125.31	2.23	110.550	300	4.10	0.51	0.81	1.60
	SSM_O_1MF_0.25ET	250.62	4.45	220.949	75	4.10	0.53	0.81	1.53
	SSM_O_1MF_0.5ET	250.62	4.45	220.949	150	4.10	0.57	0.98	1.72
	SSM_O_1MF_1ET	250.62	4.45	220.949	300	4.10	0.59	1	1.69
	Total average								1.43
	Standard deviation								0.30

4 Results and Discussions

The SFOE factor results for all specimens are presented in Table 6. A comparison of the results for the non-magnetically treated specimens is shown in Fig. 11. The factor of the uncompacted specimen was approximately 0.3, which was more than 0.2 less than that of the compacted specimen in all mortar types.

This result shows that compaction increases the SFOE factor. The fibers were aligned vertically by vibrations (around 30°). On the other hand, when comparing the results between the mortar mix types, it can be seen that the factor of the uncompacted specimen increased from 0.27 for NM to 0.3 and 0.35 for NSSM and SSM, respectively. It should be noted that the viscosity decreased in the order of NM, NSSM, and SSM. Therefore, the SFOE factor has a clear correlation with the viscosity of the mortar type. This indicates that the effect of vibration compaction to the viscosity is dominant. Because of the compaction process of the low-viscosity mortar, the steel fibers and fine aggregates segregate, which makes the steel fibers align along horizontal planes. The segregation of steel slag was visible in the compacted NSSM and SSM series. The SFOE factor enhancement will decrease as the plastic viscosity decreases. However, it can be seen that the SFOE factor after vibration compaction is only 0.56 at most. Therefore, a factor exceeding 0.56 is considered to be a contribution from the magnetic field exposure. Table 7 compares the average results for the control specimen (NM_O, NSSM_O, and SSM_O series) SFOE factors with the predicted values from previous studies. As can be seen, there is good agreement between the results, which implies the feasibility of using the steel fiber orientation analysis (visual inspection process presented in Sect. 3.2.4).

The effects of the magnetic field exposure time at an electric current of 4.45 A (approximately 251.104 G) are depicted in Fig. 12, whereas Fig. 13 presents the effects of the magnetic induction intensity at a magnetic field exposure time of 300 s. Evidently, a longer magnetic field exposure time and larger magnetic induction intensity resulted in a significantly higher SFOE factor for the NM case, whereas for the NSSM and SSM cases, a longer magnetic field exposure time and larger magnetic induction intensity resulted in a slightly higher SFOE factor.

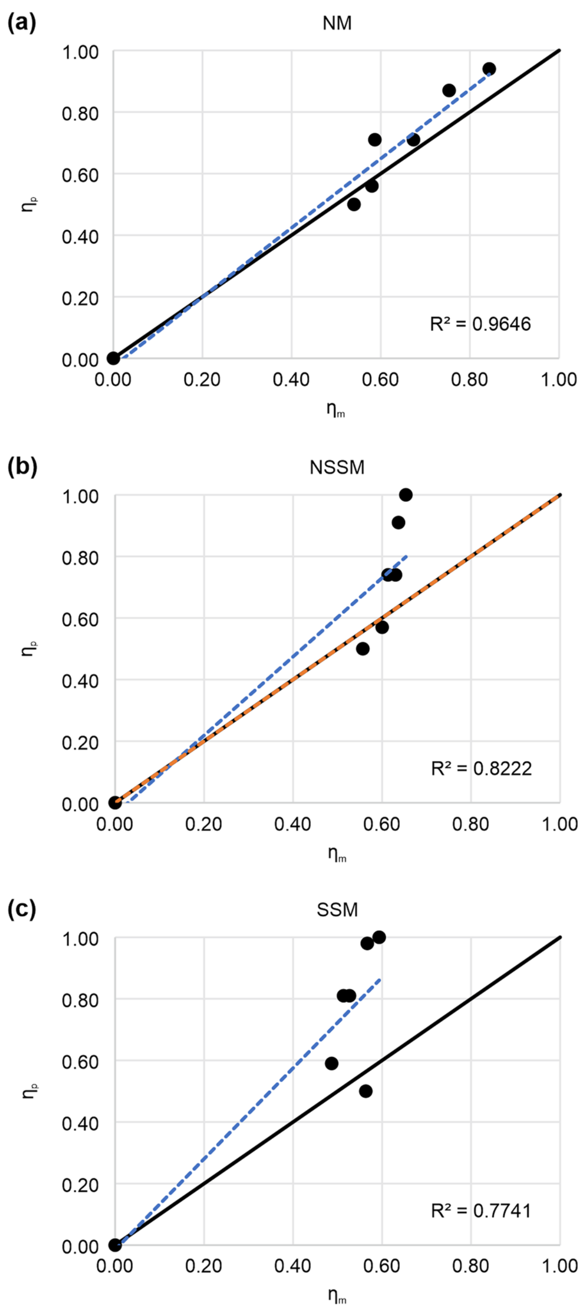

Fig. 14 Model evaluation results for each mortar mix type. **a** NM **b** NSSM **c** SSM

This result indicates that the effects of magnetic induction intensity and exposure time were not significant in NSSM and SSM compared to NM. This result contradicts the expectations. Additional investigation of the causes of these unexpected results is presented and discussed in the following section.

5 Comparison and Magnetic Field Analysis

5.1 Comparison of the Model for the SFOE Factor with Experimental Results

Table 8 lists the input values used to calculate Eqs. (6), (7), and (9), in addition to the resulting SFOE factor (η_p). The magnetic induction intensity used in the calculation of η_p is the measured intensity listed in Table 6. Similarly, for the viscosity, the measured values presented in Table 5 were used. Moreover, the experimental factor (η_m), which was obtained from the visual inspection of three specimens, is also presented for comparison in Table 8. In the case of NM, the mean and standard deviation of the values η_p were slightly overestimated at 1.07 and 0.10, respectively; however, the results are generally close to the values of η_m. On the other hand, the η_p values of NSSM and SSM were found to be overestimated by 20% and 43%, respectively, compared to η_m, and above all, the standard deviation of η_p was very large.

Fig. 14 shows the model evaluation results for each mortar mix type. As shown in the figure, the results of NM match well that the coefficient of determination between predicted (η_p) and experimental (η_m) factors exceeds 0.96. However, the coefficients of determination of NSSM and SSM are only 0.82 and 0.77. In particular, the model overestimates the SFOE factor compared to the experimental results. Consequently, the SFOE factor model proposed in this study is suitable for application to NM but not for NSSM and SSM containing ferrous materials such as steel slags. To determine the cause of this unexpected result, an electromagnetic field analysis was conducted, which is presented in the next section.

5.2 Magnetic Field Analysis

Electromagnetic field analysis was performed to identify the problem of the proposed model overestimating the SFOE factor of mortar containing ferrous materials other than steel fibers. The ANSYS Maxwell program was used to determine the magnetic-field intensity and permeability of the steel fibers. A finite-element model was developed based on the experiment, as illustrated in Fig. 15. The specimen under electromagnetic field exposure was modeled. Therefore, this model included fresh mortar, steel fibers, acrylic molds, bobbins, and coils, as shown in Fig. 15a and b. Fifteen steel fibers were modeled at the center of the specimen. In modeling, the material properties of the remaining elements except for "specimen" in Fig. 15a were given the corresponding material properties. However, the material properties of the "specimen" were modeled using the material properties of void, cement, water, sand, and steel slag, and analysis was performed for each. The models are named as control, cement, water, sand, and steel slag, as listed in Table 9.

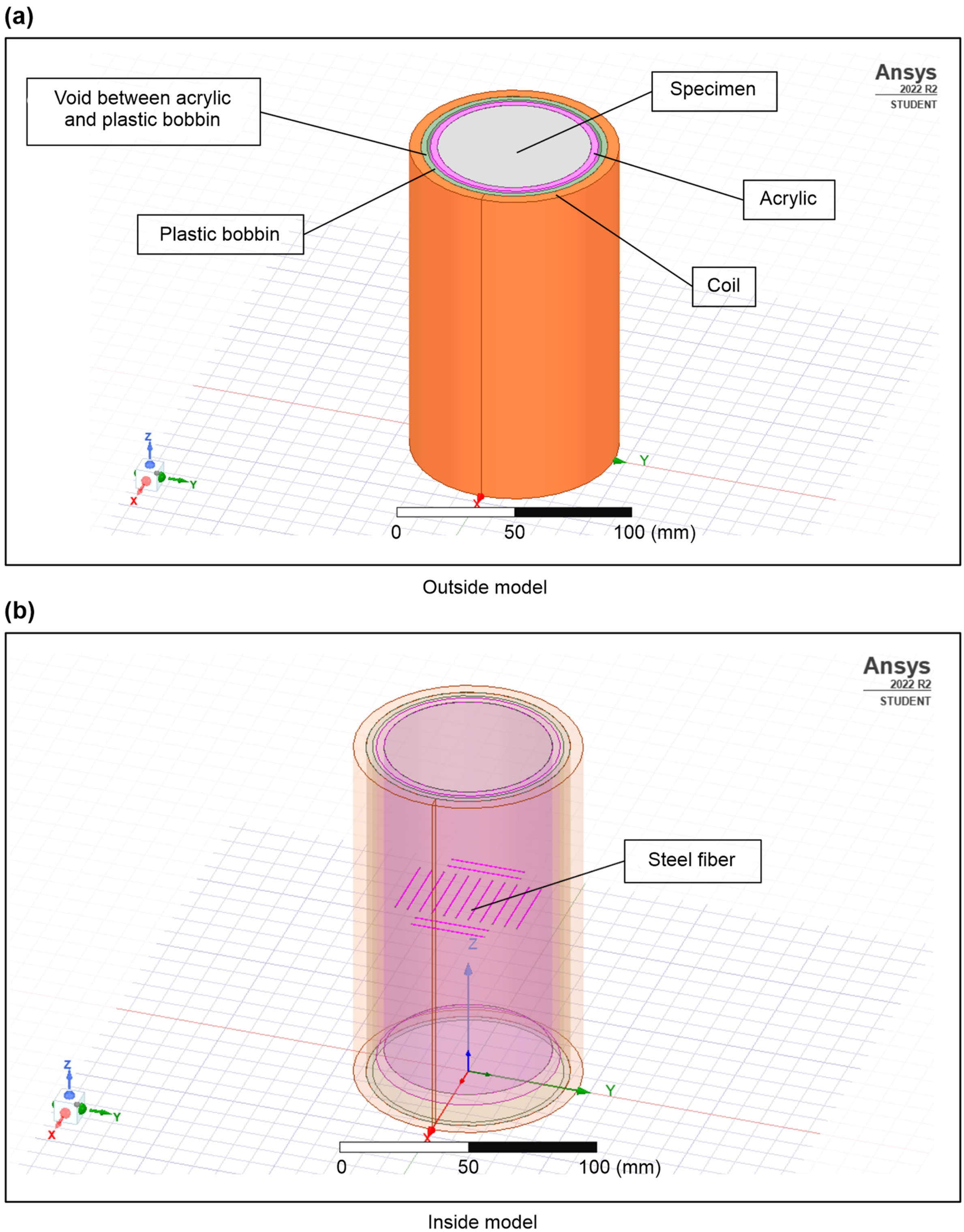

Fig. 15 Finite-element analysis model for magnetically treated specimen. **a** Outside model **b** Inside model

Table 9 Magnetic analysis results

ID	Magnetic analysis model								Mortar type					
	Cement		Water		Sand		Steel Slag		NM mortar		NSSM mortar		SSM mortar	
	B (T)	H (A/m)	B (T)	H (A/m)	B (T)	H (A/m)	B (T)	H (A/m)	B (T)	μ = B/H (N/A^2)	B (T)	μ = B/H (N/A^2)	B (T)	μ = B/H (N/A^2)
SF01	0.36	171.38	0.36	171.38	0.36	171.38	0.11	73.47	0.36	0.00209	0.30	0.00196	0.25	0.00184
SF02	0.17	107.87	0.17	107.87	0.17	107.87	0.12	76.59	0.17	0.00160	0.16	0.00158	0.15	0.00156
SF03	0.16	98.04	0.16	98.04	0.16	98.04	0.12	79.38	0.16	0.00159	0.15	0.00157	0.14	0.00155
SF04	0.35	162.84	0.35	162.84	0.35	162.84	0.11	73.82	0.35	0.00217	0.30	0.00203	0.25	0.00189
SF05	0.22	131.34	0.22	131.34	0.22	131.34	0.11	75.09	0.22	0.00169	0.20	0.00165	0.18	0.00161
SF06	0.13	84.85	0.13	84.85	0.13	84.85	0.12	79.34	0.13	0.00151	0.13	0.00151	0.12	0.00151
SF07	0.15	98.17	0.15	98.17	0.15	98.17	0.12	78.52	0.15	0.00156	0.15	0.00155	0.14	0.00154
SF08	0.18	101.97	0.18	101.97	0.18	101.97	0.12	77.08	0.18	0.00176	0.17	0.00170	0.15	0.00165
SF09	0.14	93.46	0.14	93.46	0.14	93.46	0.12	82.16	0.14	0.00151	0.14	0.00151	0.13	0.00151
SF10	0.18	119.46	0.18	119.46	0.18	119.46	0.12	80.58	0.18	0.00150	0.17	0.00150	0.15	0.00151
SF11	0.36	159.85	0.36	159.85	0.36	159.85	0.12	80.79	0.36	0.00225	0.31	0.00209	0.26	0.00193
SF12	0.28	165.85	0.28	165.85	0.28	165.85	0.12	79.63	0.28	0.00167	0.24	0.00164	0.21	0.00160
SF13	0.32	168.42	0.32	168.42	0.32	168.42	0.12	80.99	0.32	0.00188	0.27	0.00180	0.23	0.00172
SF14	0.27	157.79	0.27	157.79	0.27	157.79	0.12	79.83	0.27	0.00173	0.24	0.00168	0.21	0.00163
SF15	0.33	178.50	0.33	178.50	0.33	178.50	0.13	87.54	0.33	0.00186	0.29	0.00178	0.25	0.00171
Average									0.24	0.00176	0.21	0.00170	0.19	0.00165

Where B is the magnetic induction intensity, H is the external field, and μ is the permeability

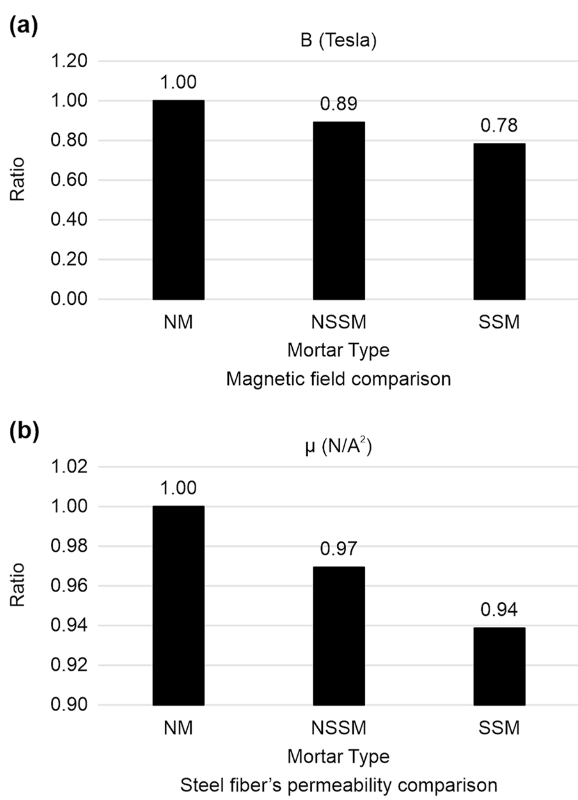

Fig. 16 Comparison results for magnetic induction intensity and steel fiber's permeability. **a** Magnetic field comparison **b** Steel fiber's permeability comparison

The current value obtained from the control model was input into the other models.

For each model, the magnetic induction intensity (B) and external field (H) acting on each steel fiber are listed in Table 9. In the table, SF1–SF15 represent the 15 steel fibers. The magnetic induction intensity and external field acting on each steel fiber differed depending on the position of the steel fiber. In the results of the cement, water, and sand models, the magnetic induction intensity acting on each steel fiber was the same, but higher than that of the steel slag model. This could be because these materials are not ferrous, such as steel slag, causing the magnetic field to bind directly to the steel fibers.

The magnetic induction intensity (B) and external field (H) acting on each steel fiber for the NM, NSSM, and SSM mortars were calculated using the output for each model (Cement, Water, Sand and Steel slag) based on the ratio of the mix compositions. The NM mortar contained 39.90% cement, 16.79% water, and 43.31% sand. The ratio of the SSM mortar was the same as that of the NM, but the ratio of sand must be replaced by the ratio of steel slag. By contrast, the NSSM mortar contained 39.90% cement, 16.79% water, 21.66% sand, and 21.66% steel slag. The calculation results are listed in Table 9 and a comparison is presented in Fig. 16. The magnetic-field intensity and permeability decreased as the steel-slag content increased. The magnetic induction intensities decreased by approximately 11% for the NSSM mortars and 22% for the SSM mortars compared with the NM mortars. The permeability decreased by 3% and 6% for the NSSM and SSM mortars, respectively, compared to the NM mortars.

The reason for the overestimation by the proposed model for NSSM and SSM can be explained by the magnetic field analysis. The decrease in the magnetic induction intensity makes it more difficult for the magnetic field to align the steel fiber, which results in a lower SFOE factor than expected. The distribution of the magnetic induction intensity in the specimen containing steel slag is more concentrated in the steel slag compared to the steel fiber because the amount of steel slag is larger than the steel fiber amount. Because the magnetic field it is expected to create a magnetic field path to a similar and closer ferrous material, which is likely between the steel slag, the magnetic induction intensity available to align the steel fibers is lower than expected.

6 Conclusion

In conclusion, this study successfully developed a prediction model for the SFOE factor in magnetically treated specimens, specifically normal mortar specimens. The model's feasibility was validated through a comparison with experimental results obtained from manual visual inspection of hardened mortar specimens. The results indicated a reasonable correlation between the predicted values from the model and the experimental data.

One notable advantage of the proposed model is its capability to predict the orientation of steel fibers under varying magnetic induction intensities and exposure durations. This distinctive feature provides valuable insights for assessing steel fiber orientation in normal mortar specimens reinforced with steel fibers and exposed to magnetic fields. However, it is important to note that the model's applicability is limited to normal mortars and may not be suitable for mortars containing ferrous materials. Electromagnetic field analysis revealed that the inclusion of ferrous materials in the mortar led to a reduction in electromagnetic intensity, thereby affecting the alignment of steel fibers. Consequently, caution should be exercised when applying the SFOE factor model proposed in this study to mortars containing ferrous materials.

In summary, the developed prediction model offers a reliable tool for estimating the SFOE factor in normal mortar specimens exposed to a magnetic field. It excels in predicting fiber orientation under specific magnetic field conditions. These findings enhance our understanding of the intricate relationship between magnetic treatment, fiber orientation, and material composition. However, further research is necessary to validate and extend the model's applicability to concrete with coarse aggregate.

Acknowledgements
This study was supported by the National Research Foundation of Korea (NRF) grant funded by the Korean Government (MIST) (No. 2020R1F1A1076566).

Author contributions
NIM: Implementation of experiments, Derive of equations. DYM: Overall research plan and control.

Funding
National Research Foundation (NRF), Republic of Korea (2020R1F1A1076566).

Availability of data and materials
Available upon request.

Declarations

Ethics approval and consent to participate
All authors of the manuscript confirm the ethics approval and consent to participate following the Journal's policies.

Consent for publication
All authors of the manuscript agree on the publication of this work in the International Journal of Concrete Structures and Materials.

Competing interests
Not applicable.

Received: 15 May 2023 Accepted: 2 September 2023
Published online: 13 February 2024

References

Alavizadeh-Farhang, A., & Silfwerbrand, J. (2000). Responses of plain and steel fiber-reinforced concrete beams to temperature and mechanical loads: Experimental study. *Transportation Research Record, 1740*(1), 25–32.

Ashare, E., Bird, R. B., & Lescarboura, J. A. (1965). Falling cylinder viscometer for non-Newtonian fluids. *AIChE Journal, 11*(5), 910–916.

Baun, M. D. (1993). Steel fiber-reinforced concrete bridge deck overlays: Experimental use by ohio department of transportation. *Transportation Research Record, 1392*, 73–78.

Chen, M. C. S., Lescarboura, J. A., & Swift, G. W. (1968). The effect of eccentricity on the terminal velocity of the cylinder in a falling cylinder viscometer. *AIChE Journal, 14*(1), 123–127.

Dupont, D., & Vandewalle, L. (2005). Distribution of steel fibres in rectangular sections. *Cement and Concrete Composites, 27*(3), 391–398.

Eichstadt, F. J., & Swift, G. W. (1966). Theoretical analysis of the falling cylinder viscometer for power law and bingham plastic fluids. *AIChE Journal, 12*(6), 1179–1183.

Ghailan, D. B., & Al-Ghalib, A. A. (1971). Magnetic alignment of steel Fibres in self-compacting concrete. *Australian Journal of Structural Engineering, 20*(4), 333–341.

Hrynyk, T. D., & Vecchio, F. J. (2014). Behavior of steel fiber-reinforced concrete slabs under impact load. *Structural Journal, 111*(5), 1213–1224.

Huang, H., Gao, X., & Khayat, K. H. (2021). Contribution of fiber alignment on flexural properties of UHPC and prediction using the composite theory. *Cement and Concrete Composites, 118*, 103971.

Kazemi, M. T., Fazileh, F., & Ebrahiminezhad, M. A. (2007). Cohesive crack model and fracture energy of steel-fiber-reinforced-concrete notched cylindrical specimens. *Journal of Materials in Civil Engineering, 19*(10), 884–890.

Khan, S., Qing, L., Ahmad, I., Mu, R., & Bi, M. (2022). Investigation on fracture behavior of cementitious composites reinforced with aligned hooked-end steel fibers. *Materials, 15*(2), 542.

Kim, J., Lee, G. P., & Moon, D. Y. (2015). Evaluation of mechanical properties of steel-fibre-reinforced concrete exposed to high temperatures by double-punch test. *Construction and Building Materials, 79*, 182–191.

Laws, V. (1971). The efficiency of fibrous reinforcement of brittle matrices. *Journal of Physics D: Applied Physics, 4*(11), 1737.

Lee, S. C., Oh, J. H., & Cho, J. Y. (2014). Fiber orientation factor on a circular cross-section in concrete members. *Journal of the Korea Concrete Institute, 26*(3), 307–313.
Lohrenz, J., Swift, G. W., & Kurata, F. (1960). An experimentally verified theoretical study of the falling cylinder viscometer. *AIChE Journal, 6*(4), 547–550.
Madandoust, R., Kazemi, M., Talebi, P. K., & de Brito, J. (2019). Effect of the curing type on the mechanical properties of lightweight concrete with polypropylene and steel fibres. *Construction and Building Materials, 223*, 1038–1052.
Michels, J., & Gams, M. (2016). Preliminary study on the influence of fibre orientation in fibre reinforced mortars. *Gradevinar, 68*(8), 645–655.
Miller, A. I., & Bjorklund, F. R. (1977). *U.S. Patent No. 4,062,913*. Washington, DC: U.S. Patent and Trademark Office.
Moon, J. S., & Kang, S. T. (2018). Prediction of tensile behavior of UHSFRC considering the flow field in the placing dominated by shear flow. *Materials, 11*(2), 194.
Mu, R., Li, H., Qing, L., Lin, J., & Zhao, Q. (2017). Aligning steel fibers in cement mortar using electro-magnetic field. *Construction and Building Materials, 131*, 309–316.
Mu, R., Qiu, X., Zhao, Q., & Li, H. (2015). Aligned steel fibre reinforced cement based composites(I): Orientation control of steel fibres. *Journal of Building Materials, 18*(2), 208–213.
Mu, R., Wei, L., Wang, X., Li, H., Qing, L., Zhou, J., & Zhao, Q. (2018). Preparation of aligned steel fiber reinforced cementitious composite and its flexural behavior. *Journal of Visualized Experiments, 136*, e56307.
Namli, M. (2021). Evaluation of the effect of using fiber reinforcement in tunnel linings for metro projects. *Underground Space, 6*(6), 732–750.
Sebaibi, N., Benzerzour, M., & Abriak, N. E. (2014). Influence of the distribution and orientation of fibres in a reinforced concrete with waste fibres and powders. *Construction and Building Materials, 65*, 254–263.
Song, Q., Yu, R., Shui, Z., Wang, X., Rao, S., Lin, Z., & Wang, Z. (2018). Key parameters in optimizing fibres orientation and distribution for Ultra-High Performance Fibre Reinforced Concrete (UHPFRC). *Construction and Building Materials, 188*, 17–27.
Soroushian, P., & Lee, C. D. (1990). Distribution and orientation of fibers in steel fiber reinforced concrete. *Materials Journal, 87*(5), 433–439.
Svedberg, B. (2004). *U.S. Patent No. 6,740,282*. Washington, DC: U.S. Patent and Trademark Office.
Valdez Aguilar, J., Juárez-Alvarado, C. A., Mendoza-Rangel, J. M., & Terán-Torres, B. T. (2021). Effect of the notch-to-depth ratio on the post-cracking behavior of steel-fiber-reinforced concrete. *Materials, 14*(2), 445.

Publisher's Note

Nur Indah Mukharromah Ph.D. student, Dong-A University, Department of Civil Engineering, Busan, Republic of Korea.

Do Young Moon Associate Professor, Kyungsung University, Department of Civil Engineering, Busan, Republic of Korea